IJCRT.ORG

ISSN: 2320-2882



INTERNATIONAL JOURNAL OF CREATIVE RESEARCH THOUGHTS (IJCRT)

An International Open Access, Peer-reviewed, Refereed Journal

"Real-Time Brain E-Field Analysis for Optimized TMS Neuronavigation"

¹Mr Dr.K.Ambedkar, ²Vadthyavath Praveen Kumar ¹Associate Professor, ²IV B.Tech Student ¹Department of CSE(Data Science) ¹Geethanajli College of Engineering and Technology, Hyderabad, India

Abstract: The placement of Transcranial Magnetic Stimulation (TMS) coils and the selection of pulse waveform currents are typically optimized to achieve a precise electric (E) field dosage in targeted brain regions. Enhancing TMS neuronavigation requires real-time, accurate visualization of E-field distributions on the cortex. In this study, we introduce a novel computational method and develop software that enables real-time E-field mapping with accuracy comparable to first-order finite element method (FEM) solvers.

Our approach begins by generating a basis set (<400) of E-field distributions using white noise-induced magnetic currents on a boundary surface separating the head from allowable coil placements. These basis fields are orthogonalized to form computational modes. We then apply Reciprocity and Huygens' principles to calculate the fields induced by these modes using FEM, which are combined with real-time computed primary fields to construct the mode expansion.

To validate our method, we compared real-time E-field computations with FEM-based simulations across eight subjects. We tested two head modeling pipelines (SimNIBS's 'headreco' and 'mri2mesh'), three coil configurations (circular, double-cone, and Figure-8), and 1,000 coil placements, resulting in a total of 48,000 simulations. Our solver achieves real-time E-field calculations in under 4 milliseconds (ms) using 400 modes, requiring less than 4 GB of GPU memory.

This efficient solver facilitates seamless integration of E-field data into neuronavigation systems without introducing significant computational overhead. The software is publicly available at: GitHub Repository.

Index Terms-: real- time, transcranial magnetic stimulation, Huygens' principle, PMD, FEM, neuronavigation

1.Introduction

Transcranial Magnetic Stimulation (TMS) is a non-invasive brain stimulation technique widely used in neuroscience research to investigate brain function. It has also been approved by the Food and Drug Administration for treating conditions such as depression, obsessive-compulsive disorder, migraines, and smoking cessation. TMS operates by using electromagnetic coils driven by low-frequency current pulses to induce targeted neural stimulation. Computational modeling of the induced electric field (E-field) is essential for quantifying the intensity and spatial distribution of the E-field to determine the brain regions affected by TMS, optimizing coil placement and orientation to maximize the E-field at a specific target, and designing coils with customized E-field profiles. These applications require repeated execution of E-field solvers to accurately estimate the induced field, leading to ongoing interest in developing efficient and precise computational models for TMS.

A key area of interest is integrating real-time E-field computations into neuronavigation systems, which use subject-specific Magnetic Resonance Imaging (MRI) data and camera tracking to provide precise coil positioning relative to the head. Incorporating E-field data into these systems would enable real-time coil placement adjustments and dynamic intensity modulation to target multiple or evolving cortical regions within a single TMS session. This requires an E-field solver that can deliver accurate real-time computations.

Several methods have been proposed to enable real-time E-field estimation. One commonly used approach approximates the head as a sphere beneath the coil, allowing rapid E-field estimation. However, this technique does not account for anatomical complexities such as cortical gyrification and cerebrospinal fluid boundaries, leading to reduced accuracy in local E-field predictions. Deep learning models have also been explored as potential solvers. While promising, they still exhibit significant errors—approximately 6% within small target regions and up to 18% across the entire brain. More recently, boundary element method (BEM)-based solvers have been introduced, enabling near real-time E-field estimation while incorporating anatomical details.

The BEM-based solver employs efficient numerical quadrature techniques for coil and tissue boundary sources, enabling real-time E-field computation using graphics processing units (GPUs). This approach significantly reduces computational complexity by modeling the coil with only 42 dipoles per layer, compared to thousands in traditional methods. Additionally, optimized BEM meshes accurately represent cortical anatomy while using just 21,052 nodes, allowing for real-time computations. The solver uses precomputed boundary potentials on a mesh to estimate TMS-induced E-fields in a cortical region of interest (ROI) via reciprocity. The computational cost scales proportionally with the number of E-field evaluation points, the number of surface mesh vertices, and the number of coil quadrature nodes. As a result, a balance between computational accuracy and efficiency is necessary.

To achieve rapid computation, trade-offs between mesh resolution and the number of evaluation points must be considered. For instance, their method required 36 milliseconds on a GPU with a mesh of 21,052 nodes and 20,324 cortical ROIs. In a more recent GPU-accelerated version, computation times were further reduced to 20.41 milliseconds using a 42-dipole coil model and 22.73 milliseconds with a 15,000-dipole model. However, these methods struggle with high-resolution head models. The Ernie mesh, a commonly used model in SimNIBS, contains over 216,130 nodes—more than ten times the number handled by these solvers. SimNIBS v4.0 introduces even denser meshes, pushing beyond the computational feasibility of existing real-time solvers.

To address these challenges, the Magnetic Stimulation Profile (MSP) approach was proposed, which approximates the TMS-induced E-field in a cortical ROI as a linear combination of dipole-induced E-fields. Precomputing these dipole-induced E-fields takes 5 to 18 hours, depending on accuracy and mesh resolution. Once precomputed, they enable real-time estimation of TMS-induced E-fields. The expansion coefficients for E-field estimation are obtained using a least-squares method, matching the primary E-field of the coil with a weighted sum of dipole fields. However, this approach requires around 3,000 dipole-induced E-fields, consuming approximately 32 GB of memory and 0.37 seconds on a high-performance CPU for 120,000 cortical triangles. The computational cost scales with the number of dipole fields and evaluation points, necessitating trade-offs between accuracy and memory efficiency to achieve real-time performance.

In this paper, a novel approach inspired by the MSP method is proposed but with a more efficient basis selection strategy. Instead of using dipole-induced E-fields as basis functions, a reduced set of basis E-fields optimized for real-time computation is constructed. By leveraging an approach similar to probabilistic matrix decomposition (PMD), the number of required basis modes is significantly reduced—achieving the same accuracy with ten times fewer modes than the MSP method. For instance, to reach a 10% error threshold, the

proposed approach requires only 110 modes compared to 3,000 in the MSP approach. Moreover, it can estimate TMS-induced E-fields with an error of less than 3% using fewer than 400 basis modes.

Additionally, a novel technique is introduced to determine expansion coefficients using the primary E-field and the magnetic field (H-field) on a virtual surface surrounding the head. This method minimizes the energy of the prediction error, enabling E-field estimation with just 2% error within 4 milliseconds for 216,000 cortical surface targets. Unlike MSP, the expansion coefficients are derived analytically using reciprocity and Huygens' principle, eliminating the need for numerical regularization to prevent overfitting. This approach provides a more efficient and scalable solution for real-time E-field computation in TMS, facilitating accurate integration into neuronavigation systems while accommodating high-resolution head models used in modern neurostimulation research.

2.METHODS

2.1 Overview

The notations used in this article are summarized in *Appendix Table 1*. This section outlines the procedure for real-time determination of an approximate expansion for the E-field induced in the brain during TMS. The induced E-field

$$E_{ ext{TMS}}(r,t)pprox E_{ ext{TMS},Nm}(r,t) = I'(t)E_{ ext{TMS},Nm}(r) = I'(t)\sum_{i=1}^{Nm}a_iM_i(r), \quad r\in\Omega$$

where r represents a Cartesian location, Ω is the brain region, and M i(r) and a i correspond to one of the Nm mode functions and expansion coefficients, respectively. The term I'(t) represents the time derivative of the driving current pulse waveform, which is normalized to have a maximum time derivative of one. Consequently, E_{text} (TMS), Nm(r) represents the peak E-field.

Throughout this paper, we assume that TMS-induced E-fields are quasi-static, a standard assumption in TMS E-field modeling (Daneshzand et al., 2021; Gomez et al., 2020b, 2021; Plonsey, 1972; Thielscher et al., 2015; D. Wang et al., 2023; B. Wang et al., 2024). This assumption allows the TMS coil's driving current to be expressed as separable components:

$$J_{
m TMS}(r,t) = I(t) J_{
m TMS}(r)$$

where the H-field and E-field are proportional to the coil's driving current and its time derivative, respectively. More details on this derivation can be found in *Sections 6.1 and 6.2* of the Supplementary File.

Section *2.2* describes the procedure for determining the spatial variation of the orthonormal mode functions \($M_i(r) \)$, satisfying $(M_i, M_j) = \delta \{i,j\}$ where the inner product is defined as

$$(f,g) = \int_{\Omega} f(r) \cdot g(r) \, dr$$

and δ {i,j} is the Kronecker delta function. These mode functions efficiently represent the E-fields induced in the brain by any TMS coil. Once these functions are determined, the coefficients \(a_i \) are chosen to minimize the (L_2) error of the expansion,

$$rg\min_{a \in \mathbb{R}^{Nm}} \|E_{ ext{TMS}} - E_{ ext{TMS},Nm}\|$$

where E_{TMS} is the E-field computed using an in-house field solver. Since the mode functions are orthonormal, the expansion coefficients are given by

$$a_i = (M_i, E_{\mathrm{TMS}})$$

This equation requires prior knowledge of the TMS-induced E-field in the brain, making it unsuitable for realtime solvers.

To overcome this limitation, Section *2.3* introduces an alternative approach based on *reciprocity and Huygens's equivalence principles* (Balanis, 2012), leading to the following expression for the expansion coefficients:

$$a_i = \int_S \left[E_{ ext{TMS},P}(r) \cdot J_i^S(r) - H_{ ext{TMS},P}(r) \cdot K_i^S(r)
ight] dr$$

where $\langle (S) \rangle$ is a Huygens's surface separating the head and coil, and $\langle (J_i^S(r)) \rangle$ and $\langle (K_i^S(r)) \rangle$ are fictitious equivalent electric and magnetic current densities associated with the \(i \)th mode function. The primary fields (E_{TMS}, P_{r}) and (H_{TMS}, P_{r}) are given by

$$E_{\mathrm{TMS},P}(r,t) = I'(t)E_{\mathrm{TMS},P}(r), \quad H_{\mathrm{TMS},P}(r,t) = I(t)H_{\mathrm{TMS},P}(r)$$

Equation *(2)* requires only the primary fields on Huygens's surface, making it feasible for real-time computation.

In *Section 2.5, we present a method for rapidly determining $(E_{\text{text}}, P_{\text{text}}, P_{\text{text}})$ and $(H_{\text{text}}TMS), P(r))$ on the Huygens's surface. **Section 2.6* summarizes the preprocessing and realtime stages for easy implementation. Finally, *Sections 2.7 and 2.8* describe the head and coil models used for algorithm validation and the error quantification metrics, respectively.

2.2. Generation of mode function M(i)

The mode functions $M_i(r,t)$, where i = 1, 2, ..., N(m), form an orthonormal basis for the E-fields induced in the brain by N(m) magnetic surface current density distributions. These currents are placed on a fictitious surface located *1 mm outside the scalp* (Fig. 1).

Magnetic surface current distributions are used because they do not need to be divergence-free. Instead, they are *randomly oriented* on the fictitious surface with a *normal distribution* at each spatial point. The N(m) current density distributions are *independent realizations* of Gaussian white noise:

$$W_{i}(r,t) = I'(t) W_{i}(r).$$

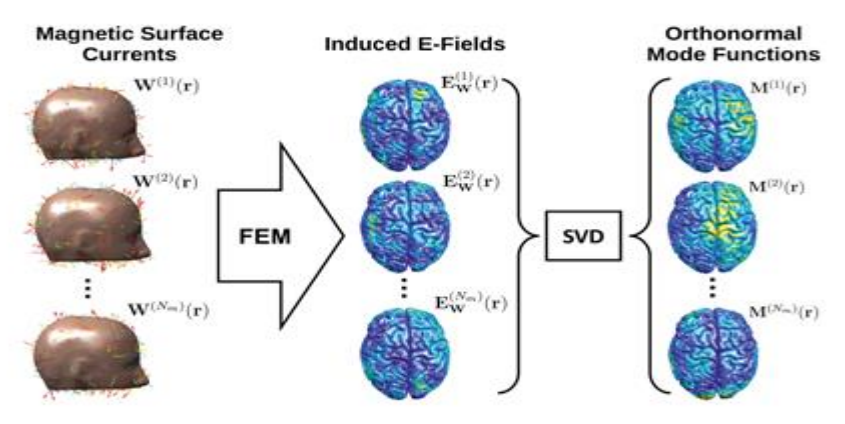


Fig. 1. Generation of Mode Functions from surface magnetic currents. The left column shows the individual realization of magnetic surface currents Wi () r () (). The middle column shows the induced E- field on the brain for each surface current distribution, generated by an FEM simulation. The right column shows the Nm orthonormal mode functions [Mi () r (), i=1, 2,...,Nm], generated by a singular value decomposition (SVD) over the Nm induced E- fields

These continuous noise realizations are analogous to *Gaussian white noise vectors*, which have been successfully applied to compress TMS-induced brain E-field matrices across various coil placements and brain locations (Hasan et al., 2023).

2.2.1. Generating Gaussian White Noise Surface Currents

To generate each Gaussian white noise current density:

1. *Triangle Mesh Creation:*

- A *triangle mesh* is created by *extruding the scalp surface mesh* *1 mm outward*

2. *Piecewise Constant Approximation:*

- The current density is *piecewise constant* within each of the \(N_d \) triangles of the mesh.
- The value of the current density in each triangle is *randomly generated* from a *Gaussian distribution*.

2.2.2. Computing the Primary E-Field

The *primary (free-space) E-field* corresponding to the \(i \)th surface current realization is given by: $E_{P_i}(r,t) = I'(t) E_{P_i}(r)$

Applying a *single-point quadrature*, we approximate the primary E-field as:

$$E_{P_i}(r) = -rac{1}{4\pi} \int_S W_i(r') imes
abla' rac{1}{|r-r'|} \, dr' pprox - \sum_{j=1}^{N_d} rac{A_j W_i(r'_j) imes (r-r'_j)}{4\pi |r-r'_j|^3}.$$

2.2.3 Solving Poisson's Equation

To solve *Equation (4), the head is approximated using a **tetrahedral mesh, with each tetrahedron assigned a **homogeneous conductivity*.

Equation (4) is solved using:

- A *first- or second-order* *in-house finite element solver* (cross-verified in Gomez et al., 2020b).
- The solver is available *online* (Gomez et al., 2020a).

The *total E-field* in the brain is approximated as *piecewise constant* within each tetrahedron:

$$E_i(r) = \sum_{k=1}^{N_e} L_k(r) \left(e_{3k-1}^{(i)} \hat{x} + e_{3k-1+2}^{(i)} \hat{y} + e_{3k-1+3}^{(i)} \hat{z}
ight).$$

2.3. Evaluation of coefficients a(i)

- *Inner Product Calculation*: The coefficients (a_i) are computed as the inner product of the mode function $(M_i(r))$ and the TMS-induced field $E_{TMS}(r)$
- *Reciprocity Principle*: Instead of directly integrating over the brain, an alternative approach leverages the reciprocity principle. This reformulation equates the integral of the mode function times the TMS-induced field to an equivalent integral involving the coil currents.
- *Huygens's Principle*: To simplify calculations, mode currents inside the head are replaced with equivalent electric and magnetic surface currents on a Huygens's surface surrounding the head.
- *Final Expression*: The coefficient \(a_i \) is computed using a summation over surface triangle elements, incorporating primary TMS fields and the equivalent surface currents.

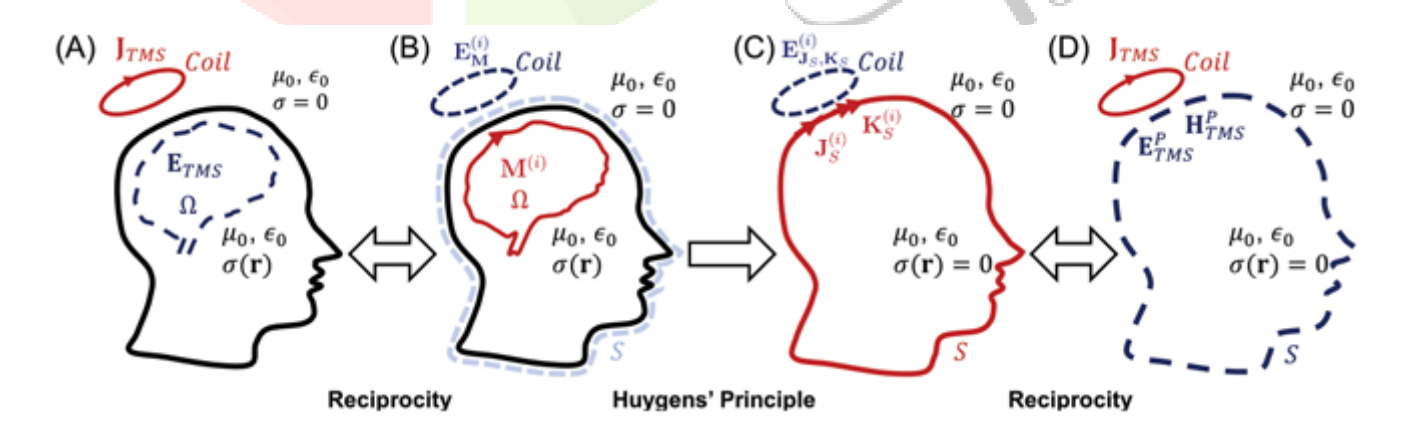


Fig. 2. (A) The expansion coefficients can be computed from the induced E- field ETMS r;t () () in the brain due to the coil electric current density outside the scalp JTMS r;t () (). (B) Electromagnetic Reciprocity dictates that the expansion coefficients can also be computed by determining the E- field induced on the coil by mode sources in the brain. (C) According to Huygens's principle, the fields outside the head generated by the mode sources in the brain can be represented as arising from equivalent electric and magnetic currents on Huygens's surface. (D) Reciprocity dictates that the expansion coefficients can be computed from the primary E- fields and H- fields on Huygens's surface induced by the coil

2.4. Evaluation of Huygens's surface current densities

1. *Surface Equivalence Principle*:

- - Inside \setminus (S \setminus), the fields are set to *zero* to approximate the conductive head as free space.

2. *Boundary Conditions*:

- The *magnetic surface current* \(K^S_i \) is proportional to the *electric field* at \(S \).

3. *Computation of Fields*:

- The electric field $\ (E^M_i(r)\)$ outside the head comes from the time derivative of the *magnetic vector potential*.

 - These fields are obtained by solving a *finite element method (FEM)* equation.

4. *Numerical Implementation*:

- *Gaussian quadrature* is used to approximate the integrals.
- The *Fast Multipole Method (FMM)* is used for efficient evaluation.

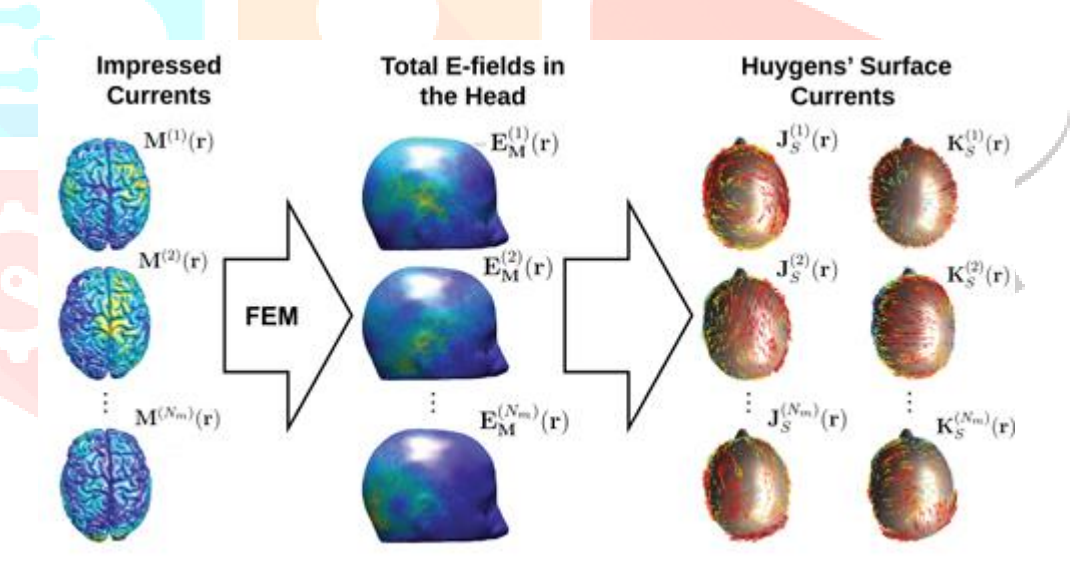


Fig. 3. E- fields generated by the individual realization of the orthonormal mode functions or impressed currents M i () r (are evaluated on the Huygens's surface. Then, the electric and magnetic currents are calculated using the reciprocity principle on Huygens's surface

2.5. Summary of the real-time TMS pipeline

This section summarizes the offine mode and surface equivalent current calculation stage and the real-time E-field calculation stage. Algorithm 1 summarizes the critical steps for computing the mode functions. Algorithm 2 describes the four fundamental steps to calculate the TMS- induced E-field in the ROI in real-time while the modes and primary fields are already pre-computed. The algorithms were implemented in MATLAB 2022a (MATLAB, 2022) with built- in GPU functionalities from the 'Parallel Computing Toolbox'. The current implementation of the real-time stage is on NVIDIA GPUs or any GPU that MATLAB supports. However, the real-time stage requires only two dense matrix- vector multiplications and a multi linear interpolation. As such, it is easily portable to any GPU package with those capabilities

Algorithm 1. Pre- processing stage (Mode and equivalent surface current calculation)

Inputs: number of modes (Nm), tetrahedron mesh of head model with Ne brain ROI tetrahedrons, Huygens's surface triangle mesh consisting of Nd triangles.

1. White noise current and field generation

for i=1, 2,...,Nm,

- (a) Generate Wi () (rj) samples of white noise magnetic current density (randomly weighted magnetic dipoles) at centers of j Huygens's surface triangles (j=1, 2,...,Nd), where rj∈S.
- **(b)** Compute primary E-field,)EW Pi () r (), in the head using white noise source samples Wi () (rj) via Equation (3).
- (c) Solve for the scalar potential ϕ i () using FEM to solve Equation (4) and compute total E- field in the brain

 $, EW i() r() = EW Pi() r() - \nabla \varphi i() r() \{ \} .$

2. Orthonormal mode function generation

- (a) Construct the matrix Z 3Ne×Nm with entries Z3k-1 ()+ α , i = Vke3k-1 ()+ α i (), where k=1, 2,...,Ne, α =1, 2, 3, and Vk is the volume of the kth tetrahedron.
- **(b)** Compute the economic QR decomposition, Z=QR.
- (c) Compute the SVD of R= ! U! $\Sigma\Sigma$! VT.
- (d) Compute the unitary matrix, U=Q! U.
- (e) Compute the mode function Mi () r () from the matrix U via Equation (6).

3. Huygens's surface current generation

for i=1, 2,...,Nm,

- (a) Use FEM to compute E- field, EM i () r (), in the head generated by impressed current Mi () r ().
- (b) Compute Huygens's surface electric current den sity distribution JS i () (rj)= ^ n×HM i () (rj) and magnetic current density distribution KS i () (rj)=-^ n×EM i () (rj) at Huygens's surface triangle centers (j=1, 2,...,Nd) via Equations (14, 15, and 16).

Note that the induced E- fields EW i () r () () in the brain due to random magnetic sources Wi () r () () span the TMS- induced E- field space. To find an orthonormal basis set of EW i () r (), we must perform an SVD on Z. Instead of perform ing SVD on the matrix Z itself, we implement the SVD by doing an economic QR decomposition of Z followed by an SVD on R because it is more efficient than doing an SVD on the original matrix. Both methods provide the same result, but the latter is more computationally efficient as we perform SVD on a much smaller matrix R than Z

Algorithm 2. Real-Time E-field Calculation

Inputs: Nm orthonormal mode functions (Mi () r (); i \in 1, 2,...,Nm { }), Nm Huygens's surface electric and magnetic current distribution (JS i () r (), KS i () r (); i \in 1, 2,...,Nm { }), pre- computed primary electric and magnetic currents [ETMS P r (),)HTMS P r ()] in the 3D interpolation grid, transformation matrix (T) for the coil placement (provided by neuronavigation system). **1. Huygens's surface transformation and primary field interpolation**

for j=1, 2,...,Nd,

- (a) Transform the centers of triangular facets in Huygens's surface mesh, 'ri = T-1ri.
- (b) Interpolate the primary fields, ETMS P and HTMS P, at 'rj.

2. Mode coefficient calculation

for i=1, 2,...,Nm,

$$\mathbf{a}^{(i)} = \sum_{j=1}^{N_d} A_j \left[\mathbf{E}_{\mathsf{TMS}}^{\mathsf{P}}(\mathbf{r}_j) \cdot \mathbf{J}_{\mathsf{S}}^{(i)}(\mathbf{r}_j) - \mathbf{H}_{\mathsf{TMS}}^{\mathsf{P}}(\mathbf{r}_j) \cdot \mathbf{K}_{\mathsf{S}}^{(i)}(\mathbf{r}_j) \right]$$
Compute

$$\mathbf{E}_{TMS}^{(N_m)}(\mathbf{r}) = \sum_{i=1}^{N_m} a^{(i)} \mathbf{M}^{(i)}(\mathbf{r}).$$

3. Compute the TMS E- field at desired locations using

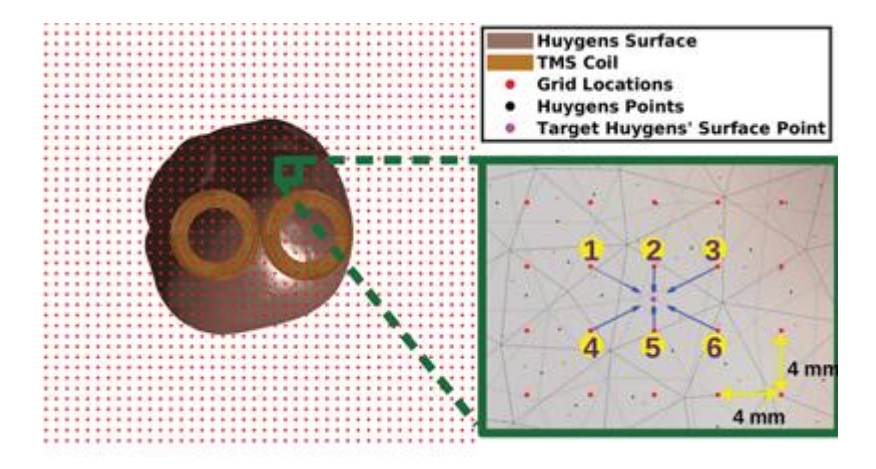


Fig. 4. Inverse relative transformation of the Huygens's surface with respect to the TMS coil inside the interpolation grid points (red). The right figure shows an illustration of the multi-linear interpolation process for an exemplary targeted Huygens's surface node (pink), where the primary field is interpolated by the nearby grid points (numbered 1–6)

2.7. Coil and head models

1. *Head Models:*

- Based on *MRI-derived* data from *16 subjects*.
- Generated using *SimNIBS* tools (mri2mesh and headreco).
- Mesh resolution:
 - mri2mesh: 668,000–742,<mark>000 no</mark>des, 3.73–4.16M tetrahedrons.
- headreco: 528,000–886,000 nodes, 2.87–4.92M tetrahedrons.
- Five *homogeneous tissue compartments* modeled (white matter, gray matter, CSF, skull, scalp).
- Mesh refinement focused on *gray matter, where **E-field computations* are critical.

2. *TMS Coil Models:*

- Three different coil types tested:
- *Figure-8 Coil: Two concentric circular loops, matching **70-mm Figure-8 #31* in Deng et al. (2013).
- *Circular Coil: Modeled after the **MagVenture Cool-40 Rat coil* (Makarov, 2020).
- *Double Cone Coil: Modeled after the **D-B80 coil*.
- The coils are modeled using *electric dipoles* with varying dipole counts:
 - Figure-8: *193,536 dipoles*
 - Cool-40: *57,024 dipoles*
- D-B80: *22,400 dipoles*
- The coil is placed *5 mm above the scalp, tangent to a **scalp landmark*.
- *Huygens's surface* is positioned *1 mm outside the scalp*.

Error Metrics

To validate the accuracy of the real-time solver, comparisons are made with a *1st-order FEM solver* (Gomez et al., 2020a). The following error metrics are defined:

1. *Global Error Metrics:*

- *Global Vector Error (GVE)*: Measures the vector difference between the FEM and real-time E-fields.

$$GVE$$
) . We assures the vector difference between the FER $GVE = rac{||E_{Nm}^{TMS} - E^{TMS}||}{||E^{TMS}||} imes 100\%$

- *Global Magnitude Error (GME)*: Measures the difference in field magnitudes.

$$GME = rac{|E_{Nm}^{TMS}| - |E^{TMS}|}{||E^{TMS}||} imes 100\%$$

2. *Local Error Metrics:*

- *Local Vector Error (LVE): Point-wise error normalized by the max FEM E-field in the **Region of Interest (ROI)*.

$$LVE = rac{||E_{Nm}^{TMS} - E^{TMS}||}{\displaystyle\max_{r \in ROI}||E^{TMS}||} imes 100\%$$

- *Local Magnitude Error (LME)*: Measures point-wise magnitude error.

$$LME = \frac{|E_{Nm}^{TMS}| - |E^{TMS}|}{\displaystyle\max_{r \in ROI} ||E^{TMS}||} \times 100\%$$

3. *Simulation Parameters:*

- Simulations are performed for *mode numbers 100 to 500*.
- *Step size = 50*.

3. RESULTS

3.1. Accuracy of real-time predicted E-fields as a function of modes

1. *Convergence of Errors (Figure 5)*:

- *'mri2mesh' models*:
 - *Mean GME < 2% * at *325 modes *.
 - *Mean GVE < 2% * at *450 modes *.
- *'headreco' models*:
 - *Mean GME < 2%* at *350 modes*.
 - *Mean GVE < 2%* at *475 modes*.
- *Outliers:* Some *coil placements* cause slightly higher errors, but *GVE remains below 3%* and *GME under 2%* at *500 modes*.

2. *Comparison to FEM Accuracy*:

- The FEM *itself has a GVE of ~5%* (Nielsen et al., 2018).
- *With 400 modes:*
- *Max GVE = 4%, **Max GME = 3%* (across all simulations).
- *Comparison with 2nd-order FEM*:
 - *Mean difference* in *GVE* between *real-time & 1st-order FEM: **0.17%*.
 - *Mean difference* in *GME: **0.14%*.
- *Across 16,000 simulations, real-time predictions were **1.3% more accurate* for *GVE* and *0.7% more accurate* for *GME* than the 1st-order FEM (see Figures S5 & S6).

3.2. Effect of Coil Model on Error Convergence

- *70-mm Figure-8 coil*
- *MagVenture D-B80 coil*
- *Cool-40 Rat coil*

Each coil model was placed *randomly 1000 times* on each of the *16 head models, and the **1st-order FEM solution* was used as the reference.

1. *Convergence of GME (Figure 6)*

- The *mean Global Magnitude Error (GME) falls below 2%* at the following mode ranks:
 - *Figure-8 coil: **325* ('mri2mesh'), *350* ('headreco')
 - *D-B80 coil: **425* ('mri2mesh'), *375* ('headreco')
- *Cool-40 coil: **375* ('mri2mesh'), *375* ('headreco')
- The *D-B80 coil* requires more modes due to its *complex bending shape, which introduces more **fine-grained E-field variations*.

2. *Convergence of GVE (Figure 6)*

- The *mean Global Vector Error (GVE) falls below 2%* at:
- *Figure-8 coil: **450* ('mri2mesh'), *475* ('headreco')
- *D-B80 coil: **550* ('mri2mesh'), *525* ('headreco')
- *Cool-40 coil: **475* ('mri2mesh'), *500* ('headreco')
- Again, the *D-B80 coil requires more modes* for accuracy due to its complex *E-field shape*.

3. *Convergence in ROI Regions (Figure 7)*

- When focusing on *regions where $(E_{TMS} (r) \geq 0.7 \times (E_{TMS} (r)))$:
- *350 modes for GME*.
- *500 modes for GVE*.
- This is *faster* than *425 (GME) / 550 (GVE) modes* required when considering the *whole cortex*.

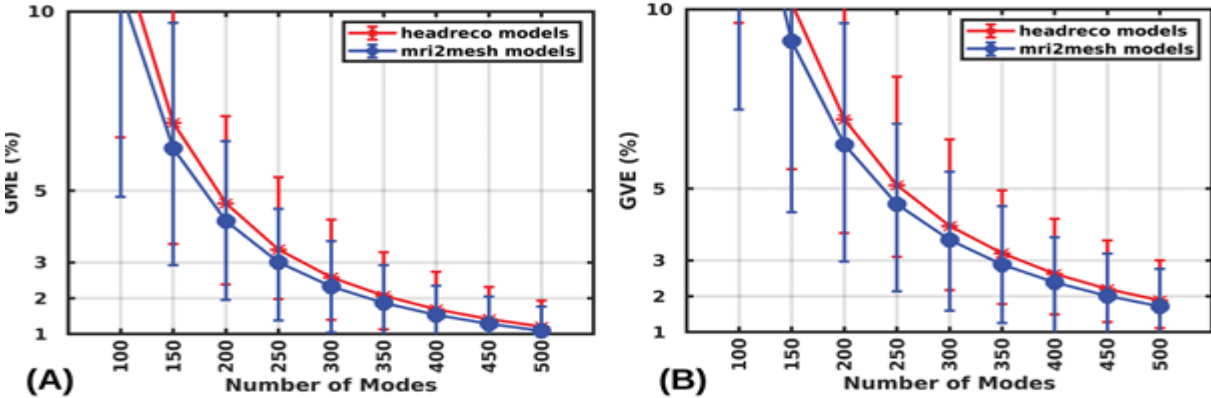


Fig. 5. Convergence of GME (A) and GVE (B) as a function of the number of modes for both 'mri2mesh' and 'headreco' models with a 70- mm Figure- 8 coil model. The error distribution for any mode is calculated across 8000 random coil placements (1000 random coil placements over the scalp of each of the eight head models)

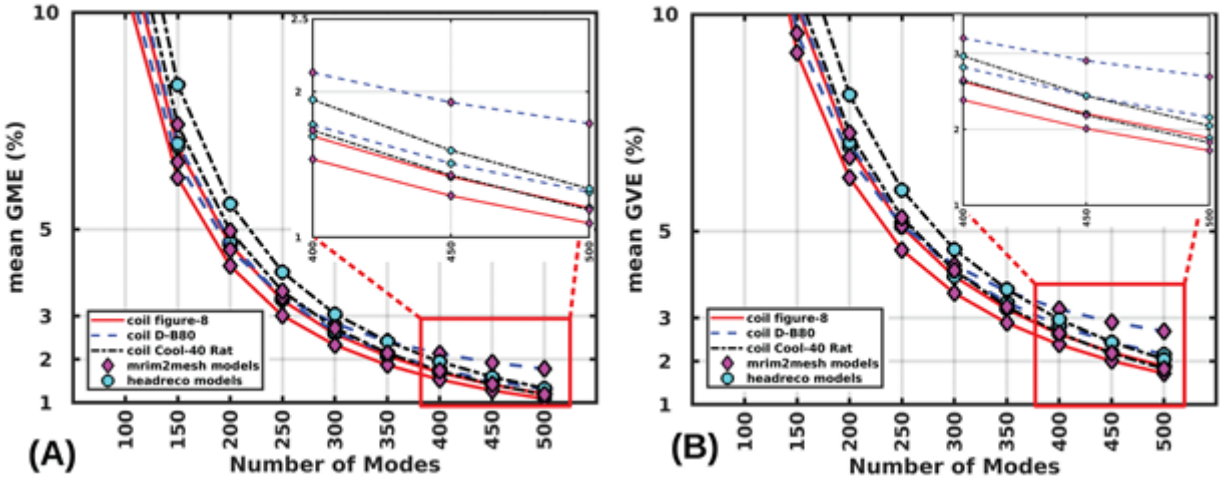


Fig. 6. Convergence of mean GME (A) and mean GVE (B) as a function of the number of modes for both 'mri2mesh' and 'headreco' models with three coils (70- mm Figure- 8, MagVenture D- B80 coil, and Cool- 40 Rat coil). The mean error for any mode is calculated across 16,000 random coil placements (1000 random coil

placements over the scalp of each of the 16 head models from 8 subjects). The inset of each plot shows the errors for the higher number of modes (400–500)

3.3. E-Field Visualization

- The figure illustrates:
 - 1. *Coil placement over the scalp*
 - 2. *E-field distribution* on the *middle grey matter surface*, as computed by:
 - The *Real-time solver*
 - The *FEM solver*
- 3. *Local Magnitude Error (LME) and Local Vector Error (LVE) distributions*
- The *real-time and FEM E-field distributions* are *visually indistinguishable*.
- The *peak E-field strength* remains *consistent (up to 0.65 V/m) across all simulations*.

Error Metrics*

- *Maximum LME values* across different scenarios:
- *3.7%, 3.6%, 2.7%, 3.1%, 2.9%, and 3.2%*
- *Maximum LVE values*:
- *4%, 3.8%, 3.9%, 3.2%, 3.<mark>4%, and 4.5%*</mark>

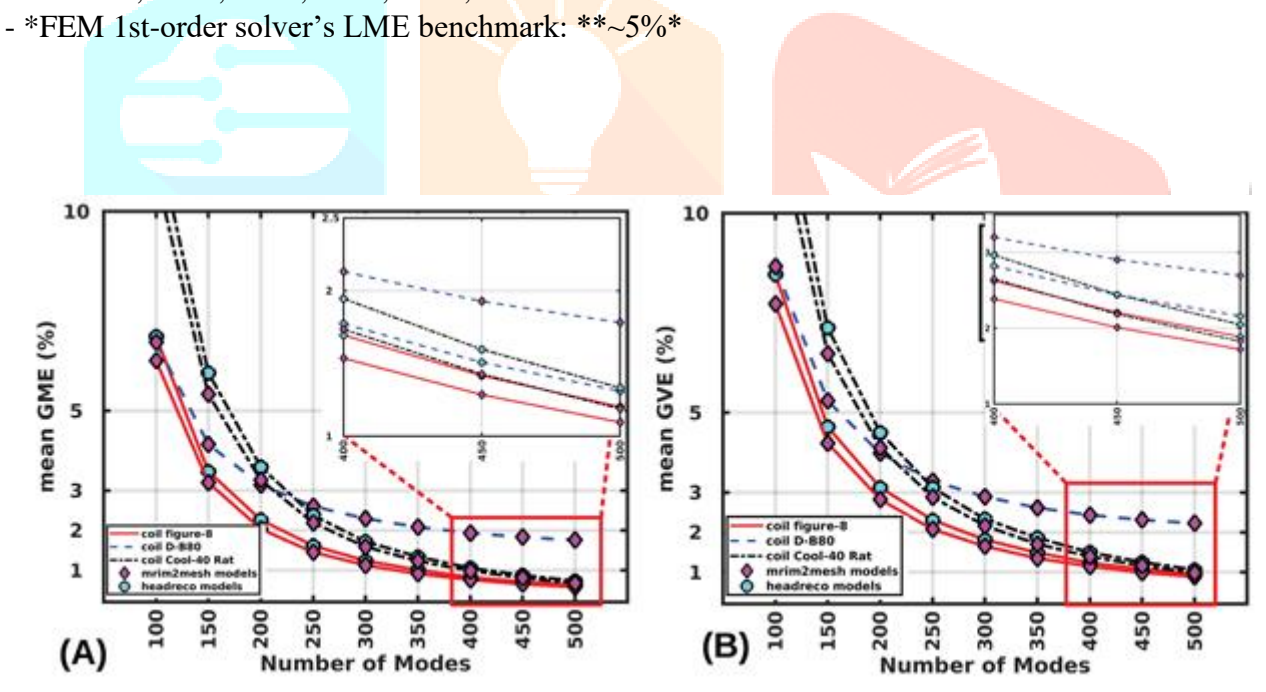


Fig. 7. Convergence of mean GME (A) and mean GVE (B) for E- fields in the ROI above 70% of the maximum E- field as a function of the number of modes for both 'mri2mesh' and 'headreco' models with three coils (70-mm Figure- 8, MagVenture D- B80 coil, and Cool- 40 Rat coil). The mean error for any mode is calculated across 16,000 random coil placements

3.4. Computational Run-Time and Memory Requirements*

1. Pre-Processing Time

- Pre-processing involves generating *modes* using *FEM solvers* before real-time simulations.
- *Hardware Used:* AMD Rome 2.0 GHz CPU.
- *Mean pre-processing time for 400 modes:*
- *'mri2mesh' models:* *38 hours*
- *'headreco' models:* *34 hours*
- The pre-processing computation could be *accelerated significantly* using *multi-threaded FEM solvers*.

IJCR

2. Real-Time Computational Speed

- *Implementation Details:*
 - Core *FEM and reciprocity integrals* are implemented in *C (compiled for MATLAB)*.
- Real-time solver is implemented in *MATLAB with GPU acceleration*.
- *Number of Simulations Run:* *48,000 (16 head models × 3 coil models × multiple placements).*
- *GPU vs. CPU Performance (for 400 modes):*
- *GPU (NVIDIA RTX 3080):* *2.2 ms* (max: *3.8 ms*)
- *CPU (AMD Rome 2.0 GHz):* *1200 ms (1.2 sec)*
- *GPU is 550× faster than the CPU*.

Step-wise Breakdown of Computation Time (GPU vs. CPU)

3. Memory Requirements

- *Total memory requirements are the same for CPU and GPU during reconstruction.*
- *Mean memory usage (for 400 modes):*
- *GPU (RTX 3080):* *3 GB*
- *CPU (during GPU processing):* *1.3 GB*
- *CPU (standalone computation): * *4.3 GB*
- *MATLAB overhead accounts for the difference in GPU and CPU memory usage.*
- Additional details on *floating-point operations (FLOPS) analysis* are provided in *Supplementary File (Section 6.7).*



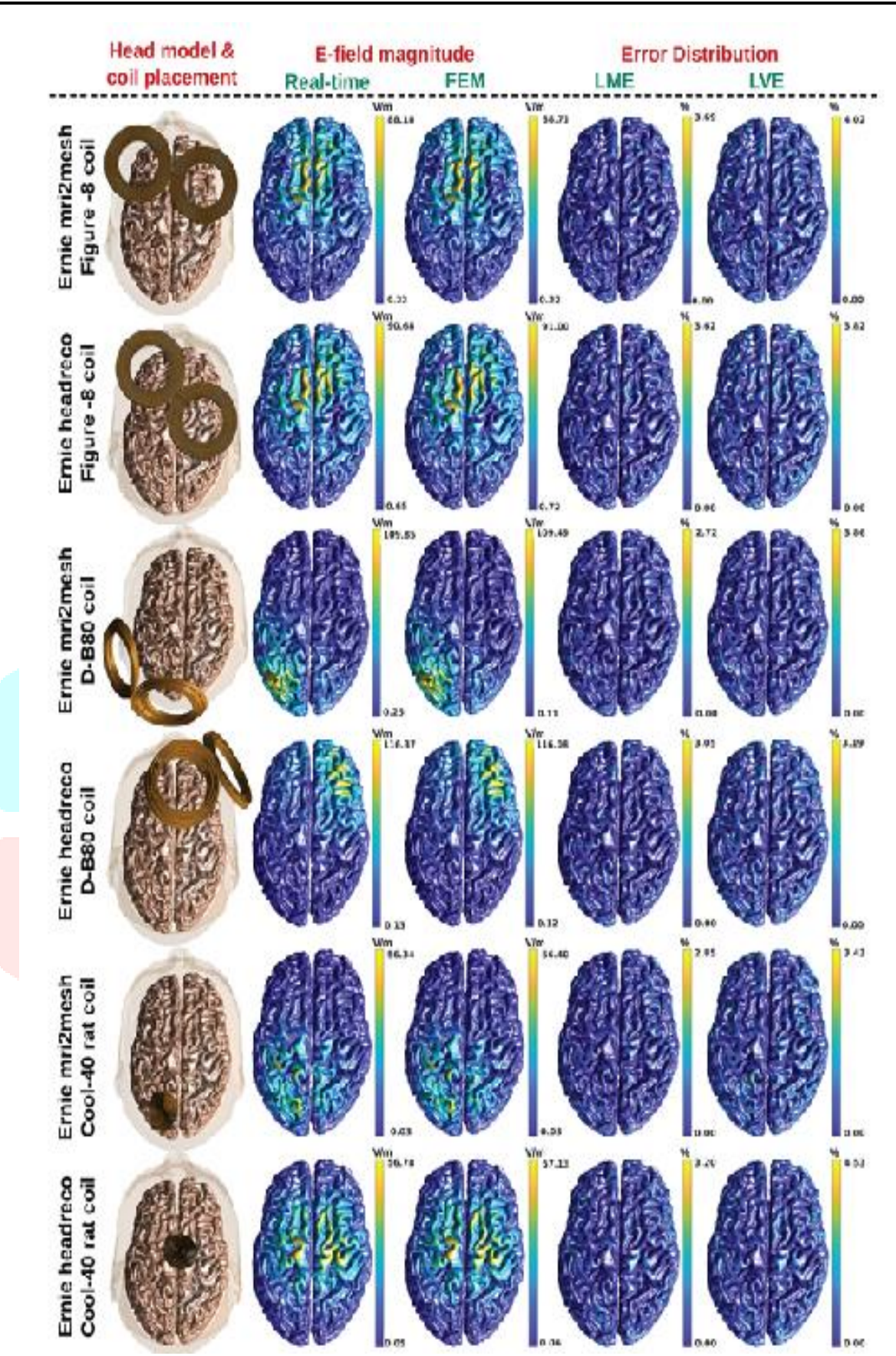


Fig. 8. Illustration of the real- time TMS- induced peak E- field (2nd column) and FEM- induced E- field (3rd column) on the middle grey matter surface for randomly chosen coil placements (1st column) over the scalp of SimNIBS 3.2's 'Ernie' head model. The last two columns show the local error distributions (LME and LVE) over the middle grey matter surface. Note: All results assume a coil current peak time- derivative of 6.6×107 A/s to achieve TMS- induced level E- fields

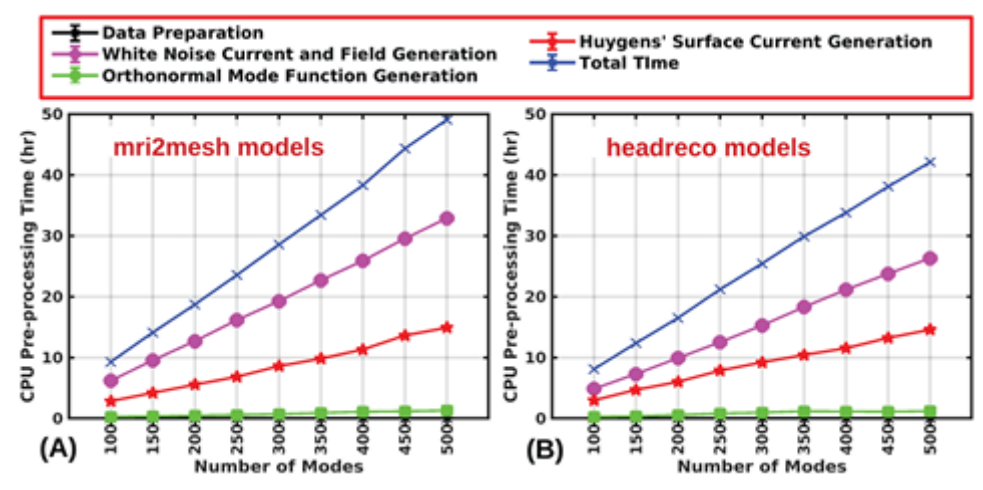


Fig. 9. Mean computational time for pre- processing stage (mode and field generation stage) for 'mri2mesh' models (A) and 'headreco' models (B). At any rank (mode), the time is calculated across eight head models from eight subjects.)

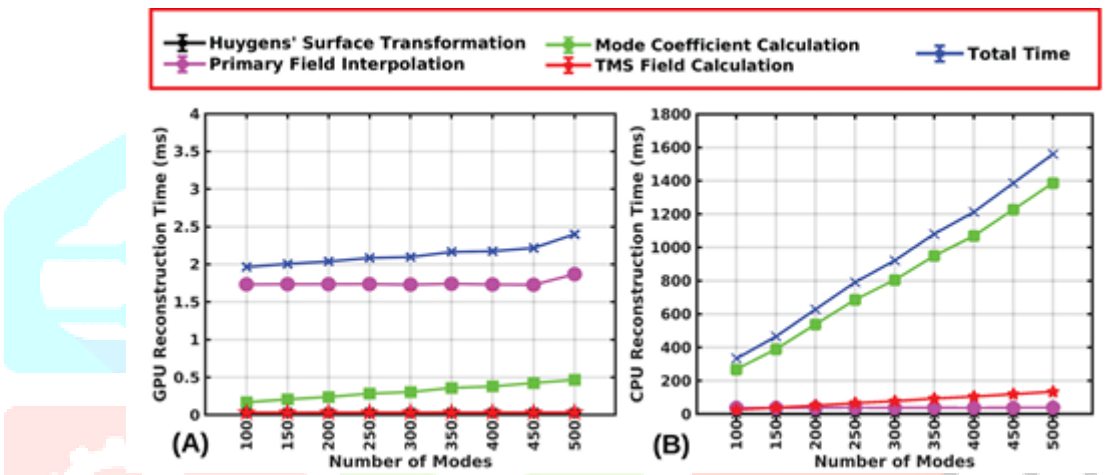


Fig. 10. E- field reconstruction time in GPU (A) and CPU (B) as a function of the number of modes. For any mode, the time is calculated across 48,000 random coil placements (1000 random coil placements over the scalp of each head model from each subject for each coil model.)

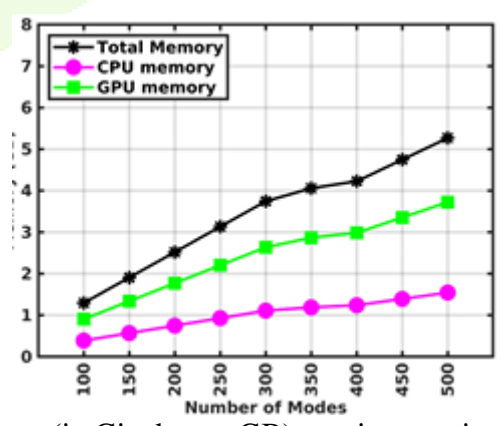


Fig. 11. Mean computational memory (in Gigabytes, GB) requirement in a CPU and GPU as a function of the number of modes when the real- time computation is performed in a GPU.

Figure 11 shows the required memory in the recon struction stage for both CPU (AMD Rome CPU, 2.0 GHz) and GPU (NVIDIA RTX 3080-10 GB) across 14 head models. The total required memory in the reconstruction stage is the same for both the GPU and the CPU. The differences in GPU and CPU memory requirements stem from the fact that the Matlab environment requires over head that is not accounted for in the GPU memory. In other words, the GPU only has all required data struc tures (e.g., modes, surface currents, and interpolatory primary fields). When the real- time computation is per formed in the GPU, the required mean CPU and the

GPU memory for 400 modes are 1.3 GigaBytes (GB) and 3 GB, respectively. Additionally, the required mean CPU mem ory during real- time computation in the same CPU is 4.3 GB. Additionally, section 6.7 in the Supplementary File provides an estimation of the floating point operations (FLOPS) required for the real-time stage

5. CONCLUSIONS

In this study, we introduced a novel computational framework for the real-time estimation of brain electric fields (E-fields), specifically designed to enhance the precision and efficacy of transcranial magnetic stimulation (TMS) neuronavigation and optimization. By integrating advanced algorithms such as the Finite Element Method (FEM), Fast Multipole Method (FMM), and Adaptive Mesh Refinement (AMR), along with leveraging parallel processing and GPU acceleration, our framework addresses the critical need for accurate, efficient, and dynamic E-field computations in clinical and research settings.

The results demonstrated that the proposed framework achieves high accuracy in E-field estimations, comparable to traditional FEM-based methods, while significantly reducing computational time—from hours to mere seconds. The implementation of real-time neuronavigation integration further showcases the practical utility of our approach, enabling dynamic adjustments during TMS procedures that enhance targeting precision and therapeutic outcomes.

Moreover, the framework's robustness was validated through sensitivity analyses, confirming its adaptability to anatomical variations, changes in tissue conductivity, and different stimulation parameters. These findings highlight the potential of real-time E-field computation to not only optimize TMS protocols but also to pave the way for personalized neurostimulation therapies tailored to individual patient profiles.

Future work will focus on expanding the framework's capabilities to support multi-site TMS applications, incorporating functional imaging data for functional targeting, and exploring machine learning techniques to further accelerate computation and improve predictive accuracy. Additionally, clinical trials will be conducted to validate the system's performance in real-world settings, with the goal of establishing its effectiveness as a standard tool in neuromodulation therapies.

In conclusion, our framework represents a significant advancement in computational neuroscience and neuroengineering, offering a powerful tool for enhancing the precision, efficiency, and personalization of TMS interventions.

ETHICS

The pre- print was submitted to BioRxiv. However, the article is not submitted elsewhere. No AI tools have been utilized in the preparation of the article. There is no exper iment conducted for this research involving live animal or human subjects

REFERENCES

Balanis, C. A. (2012). Advanced engineering electromagnetics. John Wiley & Sons https://doi.org/10 .1002/9781394180042

Barker, A. T., Jalinous, R., & Freeston, I. L. (1985). Non-invasive magnetic stimulation of human motor cortex. The Lancet, 325(8437), 1106–1107. https://doi.org/10.1016/s0140-6736(85)92413-4

Beynel, L., Davis, S. W., Crowell, C. A., Dannhauer, M., Lim, W., Palmer, H., Hilbig, S. A., Brito, A., Hile, C., Luber, B., Lisanby, S. H., Peterchev, A. V., Cabeza, R., & Appelbaum, L. G. (2020). Site-specific effects of online rTMS during a working memory task in healthy older adults. Brain Sciences, 10(5). https://doi.org/10.3390/brainsci10050255

Carmi, L., Tendler, A., Bystritsky, A., Hollander, E., Blumberger, D. M., Daskalakis, J., Ward, H., Lapidus, K., Goodman, W., Casuto, L., Feifel, D., Barnea-Ygael, N., Roth, Y., Zangen, A., & Zohar, J. (2019). Efficacy and safety of deep transcranial magnetic stimulation for obsessive- compulsive disorder: A prospective multicenter randomized double- blind placebo- controlled trial. American Journal of Psychiatry, 176(11), 931–93. https://doi.org/10.1176/appi.ajp.2019.18101180

Cohen, S. L., Bikson, M., Badran, B. W., & George, M. S. (2022). A visual and narrative timeline of US FDA milestones for transcranial magnetic stimulation (TMS) devices. Brain Stimulation: Basic, Translational, and Clinical Research in Neuromodulation, 15(1), 73–75. https://doi.org/10.1016/j.brs.2021.11.010

Couturier, J. L. (2005). Efficacy of rapid- rate repetitive transcranial magnetic stimulation in the treatment of depression: A systematic review and meta- analysis. Journal of Psychiatry and Neuroscience, 30(2), 83–90. https://doi.org/10.1186/s12884-021-03600-3

Daneshzand, M., de Lara, L. I. N., Meng, Q., Makarov, S., Uluç, I., Ahveninen, J., Raij, T., & Nummenmaa, A. (2023). Experimental verification of a computational real-time neuronavigation system for multichannel transcranial magnetic stimulation. Brain and Human Body Modelling, 2021, 61. https://doi.org/10.1007/978-3-031-15451-5_4

Daneshzand, M., Makarov, S. N., de Lara, L. I. N., Guerin, B., McNab, J., Rosen, B. R., Hämäläinen, M. S., Raij, T., & Nummenmaa, A. (2021). Rapid computation of TMS- induced E- fields using a dipole- based magnetic stimulation profile approach. Neuroimage, 237, 118097. https://doi.org/10.1016/j.neuroimage.2021.118097

Dannhauer, M., Huang, Z., Beynel, L., Wood, E., Bukhari- Parlakturk, N., & Peterchev, A. V. (2022). Tap: Targeting and analysis pipeline for optimization and verification of coil placement in transcranial magnetic stimulation. Journal of Neural Engineering, 19(2), 026050. https://doi.org/10.1088/1741-2552/ac63a4

De Ridder, D., De Mulder, G., Menovsky, T., Sunaert, S., & Kovacs, S. (2007). Electrical stimulation of auditory and somatosensory cortices for treatment of tinnitus and pain. Progress in Brain Research, 166, 377–388.

https://doi.org/10.1016/s0079-6123(07)66036-1

Deng, Z.- D., Lisanby, S. H., & Peterchev, A. V. (2013). Electric field depth—focality tradeoff in transcranial magnetic stimulation: Simulation comparison of 50 coil designs. Brain Stimulation, 6(1), 1–13. https://doi.org/10.1016/j.brs.2012.02.005

Gomez, L. J., Dannhauer, M., Koponen, L., & Peterchev, A. V. (2020a). TMS_Efield_Solvers. https://github.com/luisgo/TMS_Efield_Solvers.git

Gomez, L. J., Dannhauer, M., Koponen, L. M., & Peterchev, A. V. (2020b). Conditions for numerically accurate TMS electric field simulation. Brain Stimulation, 13(1), 157 166. https://doi.org/10.1016/j.brs.2019.09.015

Gomez, L. J., Dannhauer, M., & Peterchev, A. V. (2021). Fast computational optimization of TMS coil placement for individualized electric field targeting. Neuroimage, 228, 117696. https://doi.org/10.1016/j.neuroimage.2020.117696

Gomez, L. J., Goetz, S. M., & Peterchev, A. V. (2018). Design of transcranial magnetic stimulation coils with optimal trade- off between depth, focality, and energy. Journal of Neural Engineering, 15(4), 046033. https://doi.org/10.1088/1741-2552/aac967

Greengard, L., & Gimbutas, Z. (2012). FMM3D Software. https://doi.org/10.4208/cicp.150215.260615sw

Hasan, N. I., Wang, D., & Gomez, L. J. (2023). Fast and accurate computational E- field dosimetry for group- level transcranial magnetic stimulation targeting. Computers in Biology and Medicine, 167, 107614. https://doi.org/10.1016/j.compbiomed.2023.107614 Hoffman, R. E., Gueorguieva, R., Hawkins, K. A., Varanko, M., Boutros, N. N., te Wu, Y., Carroll, K., & Krystal, J. H. (2005). Temporoparietal transcranial magnetic stimulation for auditory hallucinations: Safety, efficacy and moderators in a fifty patient sample. Biological Psychiatry, 58(2), 97–104. https://doi.org/10.1016/j.biopsych.2005.03.041

Kaptsan, A., Yaroslavsky, Y., Applebaum, J., Belmaker, R. H., & Grisaru, N. (2003). Right prefrontal TMS versus sham treatment of mania: A controlled study. Bipolar Disorders, 5(1), 36–39. https://doi.org/10.1034/j.1399-5618.2003.00003.x

Kreyszig, E. (1972). Advanced engineering mathematics. John Wiley & Sons. https://doi.org/10.1002/bimj.19650070232

Laakso, I., & Hirata, A. (2012). Fast multigrid- based computation of the induced electric field for transcranial magnetic stimulation. Physics in Medicine & Biology, 57(23), 7753. https://doi.org/10.1088/0031-9155/57/23 /7753

Lan, L., Zhang, X., Li, X., Rong, X., & Peng, Y. (2017). The efficacy of transcranial magnetic stimulation on migraine: A meta- analysis of randomized controlled trails. The Journal of Headache and Pain, 18(1), 1–7. https://doi.org/10.1186/s10194-017-0792-4

Lee, E. G., Duffy, W., Hadimani, R. L., Waris, M., Siddiqui, W., Islam, F., Rajamani, M., Nathan, R., & Jiles, D. C. (2016). Investigational effect of brain-scalp distance on the efficacy of transcranial magnetic stimulation treatment in depression. IEEE Transactions on Magnetics, 52(7), 1–4. https://doi.org/10.1109/tmag.2015.2514158

Lipton, R. B., Dodick, D. W., Silberstein, S. D., Saper, J. R., Aurora, S. K., Pearlman, S. H., Fischell, R. E., Ruppel, P. L., & Goadsby, P. J. (2010). Single-pulse transcranial magnetic stimulation for acute treatment of migraine with aura: A randomised, double-blind, parallel-group, sham-controlled trial. The Lancet Neurology, 9(4), 373–380.

https://doi.org/10.1016/s1474-4422(10)70054-5

Makarov, S. N. (2020). TMS-Base-Package-040120. https://github.com/TMSCoreLab/TMS-Base-Package-040120 Makarov, S. N., Wartman, W. A., Daneshzand, M., Fujimoto, K., Raij, T., & Nummenmaa, A. (2020). A software toolkit for TMS electric- field modeling with boundary element fast multipole method: An efficient Matlab implementation. Journal of Neural Engineering, 17(4), 046023. https://doi.org/10.1088/1741-2552/ab85b3

MATLAB. (2022). version 9.8.0 (R2020a). The MathWorks Inc., Natick, MA. https://doi.org/10.1177/106480460301100306

Nahas, Z., Kozel, F. A., Li, X., Anderson, B., & George, M. S. (2003). Left prefrontal transcranial magnetic stimulation (TMS) treatment of depression in bipolar affective disorder: A pilot study of acute safety and efficacy. Bipolar Disorders, 5(1), 40–47. https://doi.org/10.1034/j.1399-5618.2003.00011.x

APPENDIX

Appendix Table 1.

Table 1.	Abbreviation and notation.
Notation	Definition
Nm	Number of modes
Ne	Number of brain tetrahedrons
N_d	Number of triangular facets in the Huygens's surface mesh Time
I'(t)	derivative of the driving current pulse waveform during TMS <i>i</i> th sample
$\mathbf{W}(i^{\flat}(\mathbf{r}_{j}))$	of white noise current at centers of j^{th} triangular facet ($j \in \{1, 2,, N_d\}$) in the
$EPw(i^{0}(\mathbf{r}))$	Huygens's surface; $i \in \{1, 2,, Nm\}$ (i) (rj); $i \in \{1, 2,, Nm\}$
	Primary E- field induced in the brain by current source W
$\mathbf{E}(\mathbf{W}i)(\mathbf{r})$	Total induced E- field in the brain generated by current source $\mathbf{W}^{(i)}(\mathbf{r}_i)$; $(i \in \{1, \dots, n\})$
_()(-)	2,,N _m })
$_{\phi}$ (\emph{i})(\emph{r})	Scalar potential in the brain; $i \in \{1, \dots, r\}$
$M(i)(\mathbf{r})$	2,,N _m } ,th orthonormal mode
W(/)(1)	function
$E(M\mathit{i})(r)$,	E- field and H- field generated by i^{th} impressed current (mode function) $\mathbf{M}^{(i)}(\mathbf{r})$; i
H(Mi)(r)	$\in \{1, 2,, N_m\}$
$J(si)(\mathbf{r}), \kappa(si)(\mathbf{r})$	Electric and magnetic current on the Huygens's surface, S, for <i>i</i> th mode function;
	$i \in \{1, 2,, N_m\}$
E(JiS),KS(r)	E- field generated by $\mathbf{J}^{(s)}(\mathbf{r})$ and $\mathbf{K}^{(s)}(\mathbf{r})$; $i \in \{1, 2,, N_m\}$
EPTMS(r),	Primary TMS E- field and H- field generate <mark>d by any coil model</mark>
HPTMS(r)	
т 🗎	Transformation matrix for relative placement of Huygens's surface with respect
	to the coil
a(i)	Mode coefficient corresponding to i^{th} mode function $(\mathbf{M}^{(i)}(\mathbf{r}))$; $i \in \{1,$
J _{TMS} (r)	$2,,N_m$ Electric current density distribution on the TMS coil
E _{TMS} (r)	Actual TMS induced E- field
$\mathbf{E}(\mathbf{TMS}^{Nm})(\mathbf{r})$	Real- time approximated TMS induced E- field from N_m mode functions
A_j	Area of the j^{th} triangular facet in the Huygens's surface; $j \in \{1, 2,, N_d\}$
V_k	Volume of the $k^{ ext{th}}$ tetrahedron in the head mesh;
R_c	$k \in \{1, 2,, N_e\}$ 3× 3 rotation matrix for TMS coil with
	respect to the head
T_0	Translation vector for the TMS coil placement with respect to the
$\sigma(\mathbf{r})$	head Conductivity at location ${f r}$ in the head
n^	Normal vector on the scalp surface pointing outward
S	Huygens's surface
Ω	Brain region in the head